J. Am. Ceram. Soc., **88** [6] 1669–1672 (2005)
DOI: 10.1111/j.1551-2916.2005.00319.x

Journal

A Phase Diagram for Epitaxial $PbZr_{1-x}Ti_xO_3$ Thin Films at the Bulk Morphotropic Boundary Composition

Samrat Choudhury†, Yulan Li, and Long-Qing Chen

Department of Materials Science and Engineering, The Pennsylvania State University, University Park, Pennsylvania 16802

A phase diagram of temperature versus strain was constructed for a (001)-oriented $PbZr_{1-x}Ti_xO_3$ epitaxial single crystal thin film near the bulk morphotropic boundary composition ($x = 0.47$) on an (001)-oriented cubic substrate. The phase-field approach is employed. It is shown that a mixture of distorted rhombohedral, orthorhombic, and tetragonal phases exists under small values of strain, i.e., close to the in-plane clamped boundary condition. This result contradicts thermodynamic calculations assuming a single-domain state that predicted a single distorted rhombohedral phase under similar strains. Furthermore, it is demonstrated that under a large tensile strain current phase-field simulations showed a tetragonal phase with a_1/a_2 twin structures as the stable state whereas thermodynamic calculations predicted an orthorhombic phase.

I. Introduction

Epitaxial $PbZr_{1-x}Ti_xO_3$ (PZT) thin films find wide applications in microwave acoustic devices, dynamic random access memories, and ferroelectric random access memories.[1,2] Recently considerable attention has been paid to the preparation of epitaxial PZT thin films on a wide variety of substrates such as $LaAlO_3$, MgO, Nb-doped STO,[2] $La_{05}Sr_{0.5}CoO_3$ layer on $LaAlO_3$,[3] and STO using a $SrRuO_3$ buffer layer.[4] In particular, epitaxially oriented PZT thin films[2,5–7] have been grown for compositions near the morphotropic phase boundary (MPB) as high dielectric and electromechanical properties are obtained for bulk polycrystalline ceramics near the MPB. There is growing evidence, both experimentally[4,8] and theoretically[9–11] that phase stability in PZT thin films can be significantly different from the corresponding bulk because of the presence of strains imposed by a substrate. For example, we recently obtained a temperature-composition phase diagram for PZT film under a few representative strains using the phase-field approach,[11] which showed a dramatic difference from the corresponding stress-free bulk phase diagram.

The objective of this work is to construct a temperature–strain phase diagram, i.e., the types of stable phases and domain structures as a function of strain and temperature, for epitaxial PZT thin films with a particular composition near the bulk morphotropic boundary ($x = 0.47$). The emphasis will be on both the qualitative and quantitative differences between the temperature–strain diagram obtained in this work using the phase-field approach and that predicted by thermodynamic calculations[10] which assume a single-domain state for all the ferroelectric phases. Particularly, the present phase-field simulations demonstrate that mixtures of ferroelectric phases can exist under certain strains and temperatures and that the formation of domain structures can change the relative stability of different ferroelectric phases, e.g., the relative stability of an orthorhombic phase and the tetragonal *a* domain phase under a large tensile strain.

II. Phase-Field Model

In the phase-field approach the spontaneous polarization $\mathbf{P} = (P_1, P_2, P_3)$ is chosen as the order parameter. Its evolution with time can be described by the Ginzburg–Landau equations

$$\frac{\partial P_i(\mathbf{x}, t)}{\partial t} = -L\frac{\delta F}{\delta P_i(\mathbf{x}, t)}, \quad i = 1, 2, 3 \tag{1}$$

where L is a kinetic coefficient which is related to the domain mobility, and F is the total free energy of the system. $\mathbf{x} = (x_1, x_2, x_3)$ denotes the spatial position and t is time. The total free energy is given by

$$F = F_{\text{bulk}} + F_{\text{elas}} + F_{\text{grad}} = \int_V \left(f_{\text{bulk}} + f_{\text{elas}} + f_{\text{grad}}\right) \mathrm{d}V \tag{2}$$

where f_{bulk}, f_{elas}, and f_{grad} are the bulk, elastic, and gradient energy densities, respectively, while V is the volume of the film. Inclusion of the gradient energy automatically takes into account the domain wall energy contribution. The dipole–dipole interaction is ignored and fully charge compensated surfaces and domain walls are assumed.

For describing a ferroelectric phase transition, the bulk free energy density is expanded using a polynomial of polarization components. In our simulation the six-order polynomial is employed,

$$\begin{aligned} f_{\text{bulk}} =& \alpha_1\left(P_1^2+P_2^2+P_3^2\right)+\alpha_{11}\left(P_1^4+P_2^4+P_3^4\right) \\ &+\alpha_{12}\left(P_1^2P_2^2+P_2^2P_3^2+P_3^2P_1^2\right)+\alpha_{111}\left(P_1^6+P_2^6+P_3^6\right) \\ &+\alpha_{112}\left[P_1^2\left(P_2^4+P_3^4\right)+P_2^2\left(P_1^4+P_3^4\right)+P_3^2\left(P_1^4+P_2^4\right)\right] \\ &+\alpha_{123}P_1^2P_2^2P_3^2 \end{aligned} \tag{3}$$

where α_1, α_{11}, α_{12}, α_{111}, α_{112}, and α_{123} are the dielectric stiffness and higher order stiffness constants under stress-free condition, and take the values of $\alpha_1 = 1.58\ (T-384.3)\times10^5\ \mathrm{C^{-2}\cdot m^2\cdot N}$, $\alpha_{11} = 6.68\times10^7\ \mathrm{C^{-4}\cdot m^6\cdot N}$, $\alpha_{12} = 1.94\times10^8\ \mathrm{C^{-4}\cdot m^6\cdot N}$, $\alpha_{111} = 1.66\times10^8\ \mathrm{C^{-6}\cdot m^{10}\cdot N}$, $\alpha_{112} = 7.58\times10^8\ \mathrm{C^{-6}\cdot m^{10}\cdot N}$, $\alpha_{123} = -3.57\times10^9\ \mathrm{C^{-6}\cdot m^{10}\cdot N}$.[12–17]

Isotropic domain-wall energy is assumed and the following gradient energy expression is employed:

$$\begin{aligned} f_{\text{grad}} =& \tfrac{1}{2}G_{11}(P_{1,1}^2+P_{1,2}^2+P_{1,3}^2+P_{2,1}^2+P_{2,2}^2+P_{2,3}^2 \\ &+P_{3,1}^2+P_{3,2}^2+P_{3,3}^2) \end{aligned} \tag{4}$$

where $P_{i,j} = \partial P_i/\partial x_j$ and G_{11} is the gradient energy coefficient.

D. W. Johnson Jr.—contributing editor

Manuscript No. 11083. Received June 3, 2004; approved December 28, 2004.
Supported by National Science Foundation under DMR-0122638 and DMR-0103354.
†Author to whom correspondence should be addressed. e-mail: sxc398@psu.edu

The elastic energy density at a given strain state is given by

$$\begin{aligned} f_{\text{elas}} &= \tfrac{1}{2} c_{ijkl} e_{ij} e_{kl} \\ &= \tfrac{1}{2} c_{ijkl} \left(\varepsilon_{ij} - Q_{ijmn} P_m P_n\right)\left(\varepsilon_{kl} - Q_{klmn} P_m P_n\right) \\ &= \tfrac{1}{2} c_{ijkl} Q_{ijmn} Q_{klst} P_m P_n P_s P_t - c_{ijkl} \varepsilon_{ij} Q_{klmn} P_m P_n \\ &\quad + \tfrac{1}{2} c_{ijkl} \varepsilon_{ij} \varepsilon_{kl} \end{aligned} \tag{5}$$

where e_{ij} and ε_{ij} denote the elastic strains and total strains measured with respect to the paraelectric cubic phase, and c_{ijkl} and Q_{ijkl} are the corresponding elastic stiffnesses and electrostrictive coefficients. It is evident from Eq. (5) that presence of strains modifies the second-order and the fourth-order terms of the bulk free energy polynomial compared with the stress-free state in Eq. (3), and hence the presence of strain affects the ferroelectric transition temperature and the stability of the individual phases. The details of the calculation of the total strain ε_{ij} in a (001)-oriented film under a biaxial strain, $\bar{\varepsilon}_{11} = \bar{\varepsilon}_{22} = e_0$ and $\bar{\varepsilon}_{12} = 0$ are described in our previous publication,[18,19] where the overbar means the volume average. The biaxial strain can be because of a thermal mismatch between a film and substrate if the film–substrate interface is incoherent or because of a lattice mismatch if the interface is coherent. Assuming an (001)-oriented film is coherent with an (001)-oriented cubic substrate, the biaxial strain is $e_0 = (a_s - a_f)/a_s$, where a_f and a_s are the lattice parameters of the thin film in the cubic paraelectric state and the substrate.

In computer simulations, Eq. (1) is numerically solved by the semi-implicit Fourier-spectral method.[20] A simulation cell of $128\Delta x \times 128\Delta x \times 36\Delta x$ with a uniform grid space $\Delta x/l_0 = 1.0$ is employed, where $l_0 = \sqrt{G_{110}/\alpha_0}$ and $\alpha_0 = |\alpha_1|_{T=25^\circ\mathrm{C}}$. G_{110} is a constant for normalizing G_{11} during simulation and relates to the grid spacing in real space (l_0). Periodic boundary conditions are applied along both the x_1 and x_2 directions. We choose the gradient energy coefficient such that $G_{11}/G_{110} = 0.4$. The corresponding width of domain wall is about $1.3\Delta x$, and the domain-wall energy density at $T = 25^\circ$C is evaluated to be about 0.60 $\alpha_0 l_0 P_0^2$ for 90° domain walls. $P_0 = 1$ C/m^2 is the polarization value used for the normalization during simulation. We choose $l_0 = 1$ nm such that the domain-wall width is about 13 Å, and then the corresponding domain-wall energy density is 0.045 J/m^2, which is close to experimental measurements.[21]

The film thickness is taken as $h_f = 20\Delta x$ and the heterogeneous elastic deformation in the substrate is limited to a distance of $h_s = 12\Delta x$ from the film/substrate interface. The elastic constants of the film and substrate are assumed to be the same and have cubic anisotropy: $c_{11} = 1.746 \times 10^{11}$, $c_{12} = 7.937 \times 10^{10}$, $c_{44} = 1.111 \times 10^{11}$ (N/m^2) or $s_{11} = 8.0 \times 10^{-12}$, $s_{12} = -2.5 \times 10^{-12}$, $s_{44} = 9.0 \times 10^{-12}$ (N$^{-1}\cdot$m^2). The non-zero electrostrictive coefficients take the values of $Q_{11} = 0.0908$, $Q_{12} = -0.0416$, $Q_{44} = 0.0387$ (C$^{-2}\cdot$m^4).[12] c_{ij}, s_{ij}, and Q_{ij} are the corresponding elastic stiffness, compliance, and electrostrictive coefficients in Voigt's notation.

III. Results and Discussions

We constructed a phase stability map of a $PbZr_{0.53}Ti_{0.47}O_3$ film as a function of both temperature and strain. The types of stable phases are analyzed from the polarization distribution at the end of a simulation that was started from an initial paraelectric state with small random perturbations. The results are summarized in Fig. 1. The open squares represent tetragonal c domains with polarization of $P_1 = P_2 = 0$, $P_3 \neq 0$. The squares with crosses inside represent the tetragonal a domains with polarization $P_1 \neq 0$, $P_2 = P_3 = 0$ (a_1 domain) and $P_2 \neq 0$, $P_1 = P_3 = 0$ (a_2 domain). It was found that the a_1 domain and a_2 domain always coexist, which releases the biaxial tensile strain.[22] In addition, a mixture of distorted rhombohedral phase, orthorhombic phase, and tetragonal phase is stabilized near the zero strain while a mixture of the orthorhombic phase ($|P_1| = |P_2| > 0$, $P_3 = 0$) and the tetragonal a domains phase exists under a large tensile strain at high temperature. In Fig. 1 the filled circles represent the transition temperature from paraelectric to the mixture of ferroelectric orthorhombic and tetragonal phases. The mixture regions are non-shaded in the figure while the shaded regions represent uniform phases. The two solid lines in the figure represent the transition temperatures from the paraelectric phase into a single tetragonal c domain or into a single orthorhombic domain predicted from a thermodynamic analysis.[19,23] They are given by

$$\begin{aligned} T &= T_0 + 2C\varepsilon_0 \frac{2Q_{12}}{s_{11} + s_{12}} e_0 = 0 \quad \text{if } e_0 \leq 0 \text{ and} \\ T &= T_0 + 2C\varepsilon_0 \frac{Q_{11} + Q_{12}}{s_{11} + s_{12}} e_0 = 0 \quad \text{if } e_0 \geq 0 \end{aligned} \tag{6}$$

where C, ε_0, and T_0 are Curie–Weiss constant, dielectric susceptibility of the vacuum, and Curie–Weiss temperature, respectively, where $T_0 = 384.3^\circ$C and $C = 3.57 \times 10^5$°C. Both the orthorhombic and the tetragonal a domains have the same transition

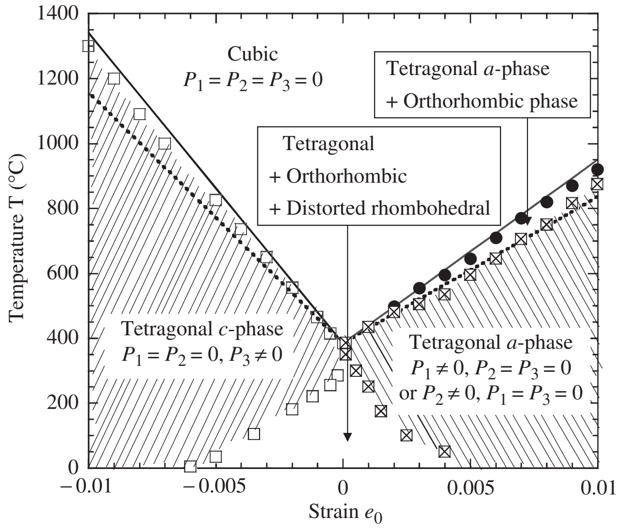

Fig. 1. Phase stability map of temperature versus strain for $PbZr_{0.53}Ti_{0.47}O_3$ epitaxial film obtained from the phase-field simulation. Squares used to demarcate the stability region of tetragonal (both a and c phases) while the filled circles represent the ferroelectric transition temperature to a mixture of tetragonal a_1/a_2 and orthorhombic phase with in-plane polarization. The solid and dashed lines delineate the transition temperatures obtained with two sets of elastic compliance constants.

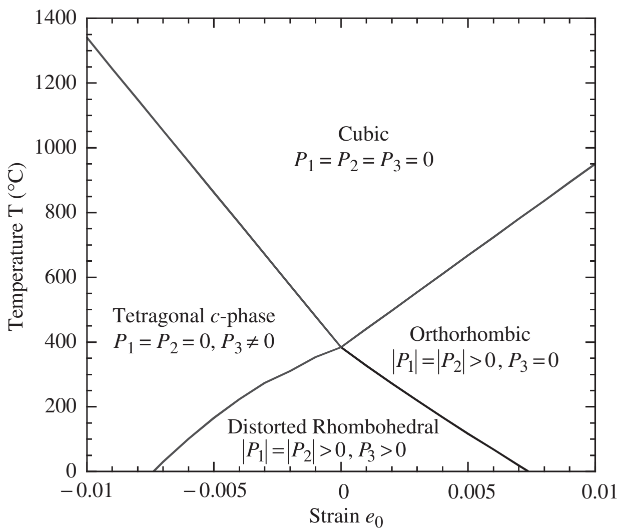

Fig. 2. Phase stability map of temperature versus strain for $PbZr_{0.53}Ti_{0.47}O_3$ epitaxial film obtained from thermodynamic calculation.

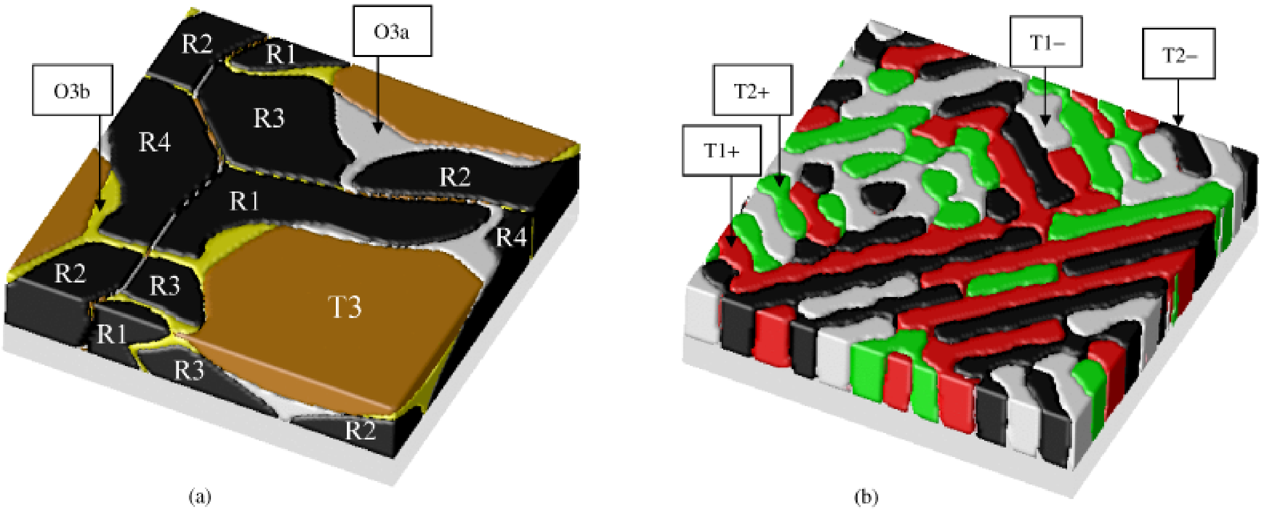

Fig. 3. Domain structures of the $PbZr_{1-x}Ti_xO_3$ ($x = 0.47$) thin film (a) at $T = 25°C$ and $e_0 = -0.005$ showing a mixture of different variants of tetragonal, distorted rhombohedral, and orthorhombic phases. R1, R2, R3, and R4 represent variants of the rhombohedral phase with polarization directions along $[\bar{1}\bar{1}\bar{1}]$, $[11\bar{1}]$, $[1\bar{1}\bar{1}]$, $[\bar{1}1\bar{1}]$, respectively, while O3a, O3b, and T3 represent variants of orthorhombic and tetragonal c phase with polarization directions along [101], [011], and [001], respectively; (b) at $T = 25°C$ and $e_0 = 0.008$ showing a twin domains of tetragonal a_1/a_2. T1+, T1−, T2+, T2− show the variants of the tetragonal phase with polarization direction along [100], $[\bar{1}00]$, [010], $[0\bar{1}0]$, respectively.

temperatures. It is obvious that the transition temperature increases with increasing strain irrespective of its nature, i.e., tensile or compressive as it has been shown previously.[19,23]

Our phase-field simulations show that tetragonal phase is stabilized under large strains regardless of whether they are tensile or compressive. This is consistent with experimental studies. It was found that under a compressive strain, the tetragonal c domain was stabilized in (001)-oriented $PbZr_{0.52}Ti_{0.48}O_3$ epitaxial thin films grown on (100) STO substrate[5] while under a tensile strain predominantly tetragonal a domains were obtained in a PZT thin film with compositions near the MPB grown on $LSCO/CeO_2/YSZ/(001)Si$[24] and MgO.[25]

As a comparison, a phase stability diagram of temperature versus strain is also calculated using thermodynamics assuming a single-domain state for all possible ferroelectric phases. The corresponding results are plotted in Fig. 2, which is essentially the same as that obtained with $x = 0.5$ previously by Pertsev *et al.*[10] Four phases are found to be stable, namely cubic ($P_1 = P_2 = P_3 = 0$), tetragonal c domain ($P_1 = P_2 = 0$, $P_3 \neq 0$), orthorhombic ($|P_1| = |P_2| > 0$, $P_3 = 0$), and distorted rhombohedral phase ($|P_1| = |P_2| > 0$, $|P_3| > 0$). A comparison of the phase diagrams obtained by the thermodynamic calculation and the phase-field simulation reveals fundamental differences. For example, under low strains, the thermodynamic calculation predicted a distorted rhombohedral phase whereas the phase-field simulation produced a mixture of distorted rhombohedral, orthorhombic, and tetragonal phases. It should be noted that a zero-strain implies an in-plane clamped boundary condition for the film. Furthermore, under a high tensile strain the thermodynamic calculation showed an orthorhombic phase as the stable phase while the phase-field simulation demonstrated that the tetragonal a domain is the most stable phase with a_1/a_2 twin structures, in agreement with experiments.[24,25] Figure 3 shows examples of domain structures in the PZT thin film at two different strains. Figure 3(a) is a mixture of tetragonal, orthorhombic, and distorted rhombohedral phases obtained under a compressive strain of $e_0 = -0.5\%$ at 25°C, where different variants of individual phases along with the polarization directions are shown. The domain walls among the different variants of the rhombohedral phase are found to be along the {100} or {110} planes, which are consistent with prior crystallographic analyses by Streiffer *et al.*[26] Figure 3(b) displays the domain structure of the tetragonal ferroelectric phase under a high tensile strain $e_0 = 0.8\%$ at room temperature. The figure shows the coexistence of the four domain variants of the tetragonal phase and the domain walls lie along the {110} planes.

To test the sensitivity of the phase diagram with respect to the model parameters, we conducted a number of systematic studies. For example, we studied the effect of the gradient energy coefficients on the phase stability diagram using a range of gradient energy coefficients $G_{11}/G_{110} = 0.2$–0.6. For this range, the calculated domain wall width and domain wall energy for 90° domains in PT lies within the theoretically and experimentally observed domain wall width and domain wall energy[21,27–29] of 5–21 Å and 0.035–0.050 J/m^2, respectively. We found that the gradient energy coefficient affects only the stability range of the mixture of the orthorhombic and tetragonal a phase, i.e., with the decrease in gradient energy coefficients the stability region of the mixture of orthorhombic and tetragonal a domains shrinks.

We also investigated the effect of elastic stiffness on the phase diagram. The elastic constants used in the simulation are those for $PbTiO_3$ at its cubic state as the elastic constant data for the single crystal cubic $PbZr_{0.53}Ti_{0.47}O_3$ is currently not available. But the elastic compliance data for $PbZr_{0.52}Ti_{0.48}O_3$ ceramic sample[30] shows that s_{11} is significantly different from the corresponding $PbTiO_3$. Pertsev *et al.*[10] used the room temperature PZT ceramics data to obtain the elastic compliance data for the cubic state. In order to study the variation of elastic compliance data on the phase stability we used the elastic compliance data corresponding to $x = 0.5$ in Pertsev *et al.*[10]: $s_{11} = 10.5 \times 10^{-12}$, $s_{12} - 3.7 \times 10^{-12}$, $s_{44} = 28.7 \times 10^{-12}$ ($N^{-1} \cdot m^2$). It was found that difference in elastic constant changes the stability region of the individual phase significantly. Firstly, at large strains, the transition temperature was lowered by $\sim$100°C. The dashed lines in Fig. 1 showed the corresponding transition temperatures by using the second set of elastic compliance data. These changes are clearly shown by Eq. (6). Moreover, the stability region of the phase mixture at low strains is reduced and is replaced by the tetragonal phase.

IV. Conclusions

A phase diagram of temperature versus strain was constructed for a (001)-oriented PZT epitaxial single crystal thin film near the bulk morphotropic boundary composition ($x = 0.47$) on an (001)-oriented cubic substrate. Under a large tensile strain a tetragonal a_1/a_2-domain structure is found to be stable except close to the transition temperatures where a mixture of orthorhombic and tetragonal phases coexist, whereas thermodynamic calculations assuming a single domain state predicted a single orthorhombic phase. Furthermore, unlike thermodynamic calculations, which predicted a single distorted rhombohedral state under low values of strains, our phase-field simulations showed a mixture of ferroelectric phases as a stable state. The stability of the individual ferroelectric state varies considerably with the elastic constants used in simulation. The gradient energy coefficients affect the size of stability regions of the mixture states but do not qualitatively change the phase diagram.

References

[1]K. R. Udayakumar, P. J. Schuele, J. Chen, S. B. Krupanidhi, and L. E. Cross, "Thickness-Dependent Electrical Characteristics of Lead Zirconate Titanate thin Films," *J. Appl. Phys.*, **77** [8] 3981–6 (1995).

[2]K. S. Hwang, T. Manabe, T. Nagahama, I. Yamaguchi, T. Kumagai, and S. Mizuta, "Effect of Substrate Material on the Crystallinity and Epitaxy of Pb(Zr,Ti)O_3 thin films," *Thin Solid Films*, **347** [1–2] 106–11 (1999).

[3]F. Wang and S. Leppavuori, "Properties of Epitaxial Ferroelectric $PbZr_{0.56}Ti_{0.44}O_3$ Heterostructures with $La_{0.5}Sr_{0.5}CoO_3$ Metallic Oxide Electrodes," *J. Appl. Phys.*, **82** [3] 1293–8 (1997).

[4]C. M. Foster, G. R. Bai, R. Csencsits, J. Vetrone, R. Jammy, L. A. Wills, E. Carr, and J. Amano, "Single-Crystal $Pb(Zr_xTi_{1-x})O_3$ Thin Films Prepared by Metal-Organic Chemical Vapor Deposition: Systematic Compositional Variation of Electronic and Optical Properties," *J. Appl. Phys.*, **81** [5] 2349–57 (1997).

[5]J. M. Triscone, L. Frauchiger, M. Decroux, L. Mieville, O. Fischer, C. Beeli, P. Stadelmann, and G. A. Racine, "Growth and Structural Properties of Epitaxial $PbZr_xTi_{1-x}O_3$ films and $PbZr_xTi_{1-x}O_3$—Cuprate Heterostructures," *J. Appl. Phys.*, **79** [8] 4298–305 (1996).

[6]J. H. Kim, Y. Kim, A. T. Chien, and F. F. Lange, "Epitaxial Growth of $PbZr_{0.5}Ti_{0.5}O_3$ Thin Films on $SrRuO_3/SrTiO_3$ Substrate Using Chemical Solution Deposition: Microstructural and Ferroelectric Properties," *J. Mater. Res.*, **16** [6] 1739–44 (2001).

[7]I. Kanno, H. Kotera, K. Wasa, T. Matsunaga, T. Kamada, and R. Takayama, "Crystallographic Characterization of Epitaxial Pb(Zr,Ti)O_3 Films with Different Zr/Tiratio Grown by Radio-Frequency-Magnetron Sputtering," *J. Appl. Phys.*, **93** [7] 4091–6 (2003).

[8]S. H. Oh and H. M. Jang, "Epitaxial Pb(Zr,Ti)O_3 Thin Films with Coexisting Tetragonal and Rhombohedral Phases," *Phys. Rev. B: Condens. Matter*, **63** 132101-1-4 (2001).

[9]S. H. Oh and H. M. Jang, "Two-Dimensional Thermodynamic Theory of Epitaxial Pb(Zr,Ti)O_3 Thin Films," *Phys. Rev. B: Condens. Matter*, **62** 14757–65 (2000).

[10]N. A. Pertsev, V. G. Kukhar, H. Kohlstedt, and R. Waser, "Phase Diagrams and Physical Properties of Single-Domain Epitaxial $Pb(Zr_{1-x}Ti_x)O_3$ Thin Films," *Phys. Rev. B: Condens. Matter*, **67** 054107-1-10 (2003).

[11]Y. L. Li, S. Choudhury, Z. K. Liu, and L. Q. Chen, "Effect of External Mechanical Constraints on the Phase Diagram of Epitaxial $PbZr_{1-x}Ti_xO_3$ Thin Films—Thermodynamic Calculations and Phase-Field Simulations," *Appl. Phys. Lett.*, **83**, 1608–10 (2003).

[12]M. J. Haun, "Thermodynamic Theory of the Lead Zirconate–Titanate Solid Solution System"; Ph.D. Thesis, The Pennsylvania State University, 1988.

[13]M. J. Haun, E. Furman, S. J. Jang, and L. E. Cross, "Thermodynamic Theory of the Lead Zirconate–Titanate Solid Solution System, Part I: Phenomenology," *Ferroelectrics*, **99**, 13–25 (1989).

[14]M. J. Haun, E. Furman, H. A. McKinstry, and L. E. Cross, "Thermodynamic Theory of the Lead Zirconate–Titanate Solid Solution System, Part II: Tricritical Behavior," *Ferroelectrics*, **99**, 27–44 (1989).

[15]M. J. Haun, Z. Q. Zhuang, E. Furman, S. J. Jang, and L. E. Cross, "Thermodynamic Theory of the Lead Zirconate–Titanate Solid Solution System, Part III: Curie Constant and Sixth-Order Polarization Interaction Dielectric Stiffness Coefficients," *Ferroelectrics*, **99**, 45–54 (1989).

[16]M. J. Haun, E. Furman, T. R. Halemane, and L. E. Cross, "Thermodynamic Theory of the Lead Zirconate–Titanate Solid Solution System, Part IV: Tilting of the Oxygen Octahedra," *Ferroelectrics*, **99**, 55–62 (1989).

[17]M. J. Haun, E. Furman, S. J. Jang, and L. E. Cross, "Thermodynamic Theory of the Lead Zirconate–Titanate Solid Solution System, Part V: Theoretical Calculations," *Ferroelectrics*, **99**, 63–86 (1989).

[18]Y. L. Li, S. Y. Hu, Z. K. Liu, and L. Q. Chen, "Phase-Field Model of Domain Structures in Ferroelectric Thin Films," *Appl. Phys. Lett.*, **78** [24] 3878–80 (2001).

[19]Y. L. Li, S. Y. Hu, Z. K. Liu, and L. Q. Chen, "Effect of Substrate Constraint on the Stability and Evolution of Ferroelectric Domain Structures in Thin Films," *Acta Mater.*, **50** [2] 395–411 (2002).

[20]L. Q. Chen and J. Shen, "Applications of Semi-Implicit Fourier Spectral Method to Phase-Field Equations," *Comput. Phys. Commun.*, **108** [2–3] 147–58 (1998).

[21]S. Stemmer, S. K. Streiffer, F. Ernst, and M. Ruhle, "Atomistic Structure of 90° Domain Walls in Ferroelectric $PbTiO_3$ Thin Films," *Philos. Mag. A*, **71** [3] 713–24 (1995).

[22]A. L. Roytburd, S. P. Alpay, L. A. Bendersky, V. Nagarajan, and R. Ramesh, "Three-Domain Architecture of Stress-Free Epitaxial Ferroelectric Thin Films," *J. Appl. Phys.*, **89** [1] 553–6 (2001).

[23]N. A. Pertsev, A. G. Zembilgotov, and A. K. Tagantsev, "Effect of Mechanical Boundary Conditions on Phase Diagrams of Epitaxial Ferroelectric Thin Films," *Phys. Rev. Lett.*, **80** [9] 1988–91 (1998).

[24]T. Kiguchi, N. Wakiya, K. Shinozaki, and N. Mizutani, "HRTEM Investigation of the 90° Domain Structure and Ferroelectric Properties of Multi-Layered PZT Thin Films," *Microelec. Eng.*, **66** [1–4] 708–12 (2003).

[25]R. Takayama and Y. Tomita, "Preparation of Epitaxial $Pb(Zr_xTi_{1-x})O_3$ Thin-Films and Their Crystallographic, Pyroelectric and Ferroelectric Properties," *J. Appl. Phys.*, **65** [4] 1666–70 (1989).

[26]S. K. Streiffer, C. B. Parker, A. E. Romanov, M. J. Lefevre, L. Zhao, J. S. Speck, W. Pompe, C. M. Foster, and G. R. Bai, "Domain Patterns in Epitaxial Rhombohedral Ferroelectric Films. I. Geometry and Experiments," *J. Appl. Phys.*, **83** [5] 2742–53 (1998).

[27]M. Foeth, P. Stadelmann, and P. A. Buffat, "Quantitative Determination of the Thickness of Ferroelectric Domain Walls Using Weak Beam Transmission Electron Microscopy," *Ultramicroscopy*, **75** [4] 203–13 (1999).

[28]B. Meyer and D. Vanderbilt, "*Ab Initio* Study of Ferroelectric Domain Walls in $PbTiO_3$," *Phys. Rev. B: Condens. Matter*, **65** 104111-1-11 (2002).

[29]F. Tsai, V. Khiznichenko, and J. M. Cowley, "High-Resolution Electron Microscopy of 90° Ferroelectric Domain Boundaries in $BaTiO_3$ and $Pb(Zr_{0.52}Ti_{0.48})O_3$," *Ultramicroscopy*, **45** [1] 55–63 (1992).

[30]Z. Q. Zhuang, M. J. Haun, S. J. Jang, and L. E. Cross, "Composition and Temperature-Dependence of the Dielectric, Piezoelectric and Elastic Properties of Pure PZT Ceramics," *IEEE Trans. Ultrason. Ferroelectrics Frequency Control*, **36** [4] 413–6 (1989). □